Batteries & Supercaps

Research Article
doi.org/10.1002/batt.202100390

Chemistry Europe
European Chemical
Societies Publishing

www.batteries-supercaps.org

Unlocking the Electrochemistry and the Activation Mechanism in the Iron-Rich $Na_{0.6}Fe_{1.2}PO_4$ Phase for High-Performance Sodium-Ion Storage

Xuelian Liu+,[a] Jiande Wang+,[a] Mengyuan Du,[a] Qi Zhu,[a] Koen Robeyns,[a] Xiaozhe Zhang,[a] Varun Kumar,[a] Jean-François Gohy,[a] Yann Garcia,[a] and Alexandru Vlad*[a]

Sodium-ion batteries are considered as the immediate sustainable alternative to lithium-ion systems. To reduce the competitiveness gap, improved performances and better understanding of sodium storage, especially of new phases based on sustainable materials, are further required. In this work, we provide advanced investigation of the structure and the electro-chemistry of a peculiar off-stoichiometric iron-rich phase ($Na_{0.6}Fe_{1.2}PO_4$) for sodium storage. An interesting electrochemical activation phenomenon is described and contrary to conventional ageing processes it is found to significantly enhance the energy and power rate performances.

Introduction

With increased efforts to achieve a sustainable development, the use of green energy such as solar, wind, and geothermal energy stands as the best solution. Nevertheless, these are intermittent, not on demand sources of electrical energy, and the establishment as well as development of better energy storage systems is imperative to deal with this discrepancy.[1] Lithium-ion batteries (LIBs) are being used for portable electronics and electric vehicles and continue to consolidate their position in the economic energy landscape.[2] However, concerns about Li and some transition metals supplies raise questions on their use for large-scale grid applications.[3] Sodium-ion batteries (SIBs), as a sustainable and cost-effective alternative technology, are attracting increasing attention[3a,4,5], and the similarity to the LIB technology progressed SIBs to an already commercial level.[6]

Whereas there are already major achievements on SIB anode materials, cathode materials remain one of the blocking elements on the way of progress. The success story of olivine $LiFePO_4$ has motivated researchers to study the electrochemistry of the Na equivalent $NaFePO_4$ phases.[7] However, opposite to olivine $LiFePO_4$, the thermodynamically stable phase of $NaFePO_4$ is the maricite, which lacks practical-level electrochemical activity.[8] Improvements have been attained by nanostructuration, or by working with the metastable Na-olivine phases, but prepared indirectly via ion exchange electrochemical routes from the olivine $LiFePO_4$. The rate capability of olivine $NaFePO_4$ remains however unsatisfactory, attributed to low electrical conductivity and slower diffusion of larger Na ions in the host materials.[9] Other Fe-based phosphate cathode materials such as $Na_2FeP_2O_7$, $Na_4Fe_3(PO_4)_2(P_2O_7)$ and $Na_3Fe_2(PO_4)_3$ have been also proposed and show promising performances.[10] Additionally, the class of off-stoichiometric Fe-phosphates ($Na_{3.12}Fe_{2.44}(P_2O_7)_2$, $Na_{3.32}Fe_{2.34}(P_2O_7)_2$, $Na_{0.71}Fe_{1.07}PO_4$)[11] provides flexibility in tuning the composition and the properties, enriching this library with novel cathode candidates.[12]

In a recent report, Yamada proposed a peculiar Fe-rich sodium phosphate phase, the $Na_{0.6}Fe_{1.2}PO_4$, to be of great interest as cathode material for Na storage.[13] This material was found to operate at an average potential of 3 V (vs. Na^+/Na), delivering a reversible capacity of 85 mAh g^{-1} (for a theoretical capacity of 91 mAh g^{-1}) at a rate of C/20 (the first cycle performance is reproduced in Figure S1A with permission from Ref. [13]). However, high polarization (and thus low energy efficiency), limited power performances, and rapid capacity loss were reported, calling for further improvements along with additional structural and mechanistic insight.

Herein, the nano-sized phase of $Na_{0.6}Fe_{1.2}PO_4$ is synthesized and enhanced electrochemical performances as compared to initial report are attained. The side reactions at high potential are reduced, the polarization is considerably diminished, and better reversibility is obtained (Figure S1B).[13] Through a series of analysis techniques we provide additional insight into the physico-chemical and electrochemical properties of this peculiar material. The galvanostatic charge-discharge behavior is evaluated in different electrolyte formulations and optimal conditions for stable cycling are provided. We also detail a peculiar electrochemical activation mechanism upon extended galvanostatic cycling, characterized by gradual appearance of a new redox process at 3.8 V (vs. Na^+/Na) accompanied by capacity increase. The activation phenomenon is independent

[a] Dr. X. Liu,+ Dr. J. Wang,+ M. Du, Dr. Q. Zhu, Dr. K. Robeyns, X. Zhang, Dr. V. Kumar, Prof. J.-F. Gohy, Prof. Y. Garcia, Prof. A. Vlad
Institute of Condensed Matter and Nanosciences
Université catholique de Louvain
Louvain-la-Neuve B-1348, Belgium
E-mail: alexandru.vlad@uclouvain.be
[+] These authors contributed equally to this work.

Batteries & Supercaps

Research Article
doi.org/10.1002/batt.202100390

Chemistry Europe
European Chemical
Societies Publishing

of the electrolyte used and current density applied, making it an interesting and promising cathode material candidate worth of further investigation on the activated phase composition and structure.

Results and Discussion

Intrigued by the interesting properties of the off-stoichiometric iron-rich material proposed by Yamada and co-workers, but also by the noticeable limitations highlighted in the original work, we aimed at further investigations and potential performance improvements.[13] The $Na_{0.6}Fe_{1.2}PO_4$ was synthesized via an improved method (refer to Experimental Section for details). The chemical composition was analyzed with inductively coupled plasma emission spectrometry and the obtained Na, Fe and P elemental ratios were found to match the theoretical values (Table S1), implying no element loss during synthesis. The powder X-ray diffraction (PXRD) pattern (Figure 1A) was indexed to a similar unit cell ($a = 14.86$ Å, $b = 6.43$ Å, $c = 10.32$ Å, $\alpha = \beta = \gamma = 90°$ and $V = 985.6$ Å^3) as of the reported one (Table S2).[13] The ^{57}Fe Mössbauer spectrum is shown in Figure 1B and the estimated parameters from fitting of isomer shift δ, quadrupole splitting ΔE_Q, half width of the lines $\Gamma/2$, and absorption area intensity ratio S are summarized in Table S3. The observed spectrum can be best fitted to four doublets. The presence of three types of Fe^{2+} sites with large values of δ (> 1.1 mm s^{-1}) and ΔE_Q (> 1.9 mm s^{-1}) associated to octahedral coordination suggests complex local environment

of Fe^{2+} ions in the crystal structure along with structural distortion. One doublet with small value of δ ($= 0.64$ mm s^{-1}) and ΔE_Q ($= 0.24$ mm s^{-1}) indicates the presence of traces of Fe^{3+} which could be due to surface oxidation of the sample during manipulation and measurements at room temperature.

Infrared spectroscopy was used to analyze the characteristic intramolecular vibration bands of the PO_4 group in $Na_{0.6}Fe_{1.2}PO_4$ (Figure 1C). The symmetric ν1 and asymmetric ν3 stretching modes appear in the high-wavenumber region (850–1200 cm^{-1}), while the intramolecular bending modes (ν2 and ν4) occur between 700 and 500 cm^{-1} in the spectrum.[14] Note that the bands in the spectrum are broadened and low-resolved, explained by the difference in atomic distances, corroborating the structural disorder.[14a,15] The broadened vibration modes are an indication of structural disorder or differences in bond distance, and are expected to play a role in the described electrochemical activation process as presented later.

The transmission electron microscopy (TEM) analysis revealed additional insight into the morphology, crystallinity and elemental distribution. The selected area electron diffraction (SAED) pattern (Figure 1D) displays interplanar rings diffraction spots with ≈0.25 and ≈0.3 nm spacing, corresponding to the (112) and (222) planes, respectively. The high-resolution TEM (HRTEM) image (Figure 1E) shows the lattice fringes in $Na_{0.6}Fe_{1.2}PO_4$ with lateral d-spacings of ≈0.52 and ≈0.27 nm, matching the (020) and (501) planes from PXRD indexing results, respectively. Morphology analysis reveals a porous nano-sized particle morphology, with small agglomerates (inset
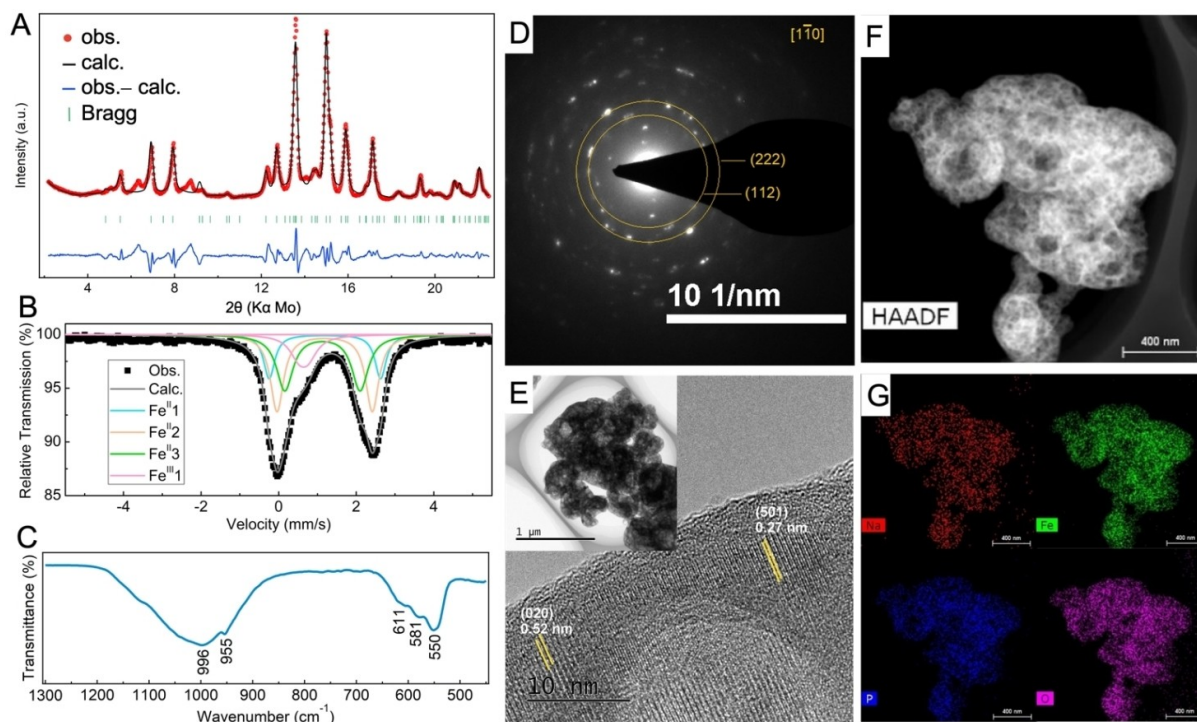

Figure 1. Physico-chemical analysis of the of the $Na_{0.6}Fe_{1.2}PO_4$ phase. A) PXRD pattern and the Rietveld refinement; B) room-temperature Mössbauer spectrum and fitting results; C) FTIR spectrum; D) SAED image; E) HRTEM with inset of TEM images; F) TEM-HAADF; and G) EDX elemental mapping for the synthesized $Na_{0.6}Fe_{1.2}PO_4$ phase.

Batteries & Supercaps

Research Article
doi.org/10.1002/batt.202100390

Chemistry
Europe

European Chemical
Societies Publishing

of Figure 1E). The porous microstructure of the particles can be also observed in the high-angle annular dark-field (HAADF) image in Figure 1(F) and the elemental mapping in Figure 1(G) further verifies uniform elemental distribution, indicating phase homogeneity.

We next focus on electrochemical analysis and discussion. It should be first noted that the galvanostatic charge-discharge performance in the initial report (Figure S1A), was accompanied by large polarization and electrolyte decomposition at high potentials. The latter is confirmed by the appearance of a plateau at high potential during charge (the dQ/dV plot displaying an irreversible anodic current above 4 V vs. Na$^+$/Na, Figure S1A). Although no additional discussion was provided by the authors, we believe this could be the main reason accounting for fast capacity decay upon cycling. To verify this, we also tested the same electrolyte formulation (1 mol NaPF$_6$ dissolved in propylene carbonate – PC with 2 vol% fluoroethylene carbonate – FEC). Our analysis also revealed low first cycle Coulombic efficiency (CE), assigned to anodic decomposition of electrolyte (Figure S2). According to these, we thus first screened a series of electrolytes to find optimal conditions for stable cycling with high CE.

The best performing electrolyte formulations found are – NaClO$_4$ in EC/DEC; NaPF$_6$ in EC/DEC; and NaClO$_4$ in EC/DEC with 5 vol% FEC. Cycling in these electrolytes eliminated the irreversible 4 V plateau, with initial capacities attaining 70 mAh g^{-1}, corresponding to 0.5 Na equivalent extracted at a rate of C/20 (1 C rate corresponds to 91 mA g^{-1}, Figures 2 and S3). The cycling stability and rate capability are also significantly improved. However, the unexpected feature was the gradual capacity increase, and more intriguing, the appearance and elongation of an additional reversible process at around 3.8 V vs. Na$^+$/Na (Figure 2A and B) accompanying the extended redox cycling.

Consequently, we performed additional long-term galvanostatic cycling tests at low and high C-rates, all providing consistent results. For example, after 110 cycles at C/20, the capacity reaches 110 mAh g^{-1}, exceeding the theoretical capacity of 91 mAh g^{-1}, in part accounted to the appearance of the 3.8 V redox event (Figure 2A). Longer-term cycling performance at 1 C and 2 C rates were also found to be excellent (while taking into account the instability of Na-metal in the used carbonate-based electrolytes).[16] Other than the significative capacity increase over the course of first 1,000 cycles (Figure 2D), the potential profiles are also significantly altered after 1,000 cycles (Figure 2C), compared to the initial potential-capacity profiles (refer also to panel 2B for significative changes noted in the dQ/dV plots with cycling). It can be noted that the shape and the length of the 3.8 V plateau is similar to one attained at a rate of C/20 (Figures 2A and S3 A, C). For the fast-cycling tests, the capacity is stabilized after about 1,000 cycles, with 97.3 and 75.5 mAh g^{-1} delivered at 1 C and 2 C, respectively, after 2,000 cycles (Figure 2D), which is comparable to slow cycling tests at C/20 (inset of Figure 2D).

The rate capability was also tested after the 2,000 cycles test (Figure 2E) and compared to the pristine material (Figure 2F). A significant improvement can be noted with

60 mAh g^{-1} retained at a rate of 5 C after activation, whereas a much lower rate of C/5 is required to reach the same capacity for the pristine material. The metrics of the thus obtained activated phase outperform many of the reported iron-based phosphate cathode materials for SIBs (Figure 2G).

An electrochemical activation processes of this type remains unusual, being rarely encountered in literature, and the origins could be various in nature, ranging from anion intercalation into the conductive carbon (however noting that the redox potential remains low for this process to be considered here);[7,17] or in-situ electrochemical fluorination as already reported, but only in oxide materials.[18] Occasionally, this has been also observed in polyanionic phosphate materials. For instance, Zhu and colleagues have disclosed a similar process in a Na$_{0.71}$Fe$_{1.07}$PO$_4$ phase.[11c] The activation process however was found to proceed faster (within 5 voltammetry cycles), and with lower contribution to the capacity increase (most probably given the lower Fe to PO$_4$ ratio, 1.07 as compared to 1.2 in this work). Although the hypothesis of extra Na$^+$ sites activation was advanced, no reaction mechanism was proposed.

To further understand the origins, we first run a series of control experiments. A blank test with only Super P carbon and poly(tetrafluoroethylene) binder (as used for the cells assembly) was cycled and no capacity increase, or redox potential profile change could be noticed (Figure S4). Thus, ruling out any significant contribution to capacity from the coin cell construct, conductive carbon or binder. To test whether the activation process is enabled by a high potential anodic process, another control experiment was performed. Using the NaClO$_4$ in EC/DEC with 5 vol% FEC as electrolyte, the cell was first charged in constant current (CC, C/20) regime, followed by a constant voltage (CV) hold at 4.4 V for 48 h, and then discharged to 1.7 V at C/20 (Figure S5A and B). Continuous cycling using this protocol revealed a similar behavior as for regular CC charge-discharge tests (Figure 2A) with the 3.8 V redox not being activated at early stages of cycling (Figure S5A).

The 3.8 V redox appeared systematically after approximately 20 cycles at C/90, 40 cycles at C/20, or around 200 cycles at 1 C (Figures 2A and S5C). To be mentioned that even before the clear emergence of this process, there is a steady increase in the capacity, accompanied by lower polarization and increase in CE (Figures 2A, D and S3). The dQ/dV analysis reveals a much more complex mechanism. The continuous evolution of redox processes at 3 V can be seen at first cycles, further evolving into a set of redox peaks at 2.6 and 2.8 V (Figure 2B). Along with this, the intensity of the peak at 3.8 V increases. A similar trend was also observed for other electrolytes, with additional features being also observed (refer to Figure S3 for a detailed discussion).

The analysis of data presented above implies that any potential anodic decomposition of the electrolyte, or other elements present in the cell are not the direct cause (although may be necessary) of the capacity increase or the appearance of the 3.8 V redox. The activation process also seems to be time and desodiation/sodiation cycles number dependent. A gradual structural modification within the pristine Na$_{0.6}$Fe$_{1.2}$PO$_4$ phase
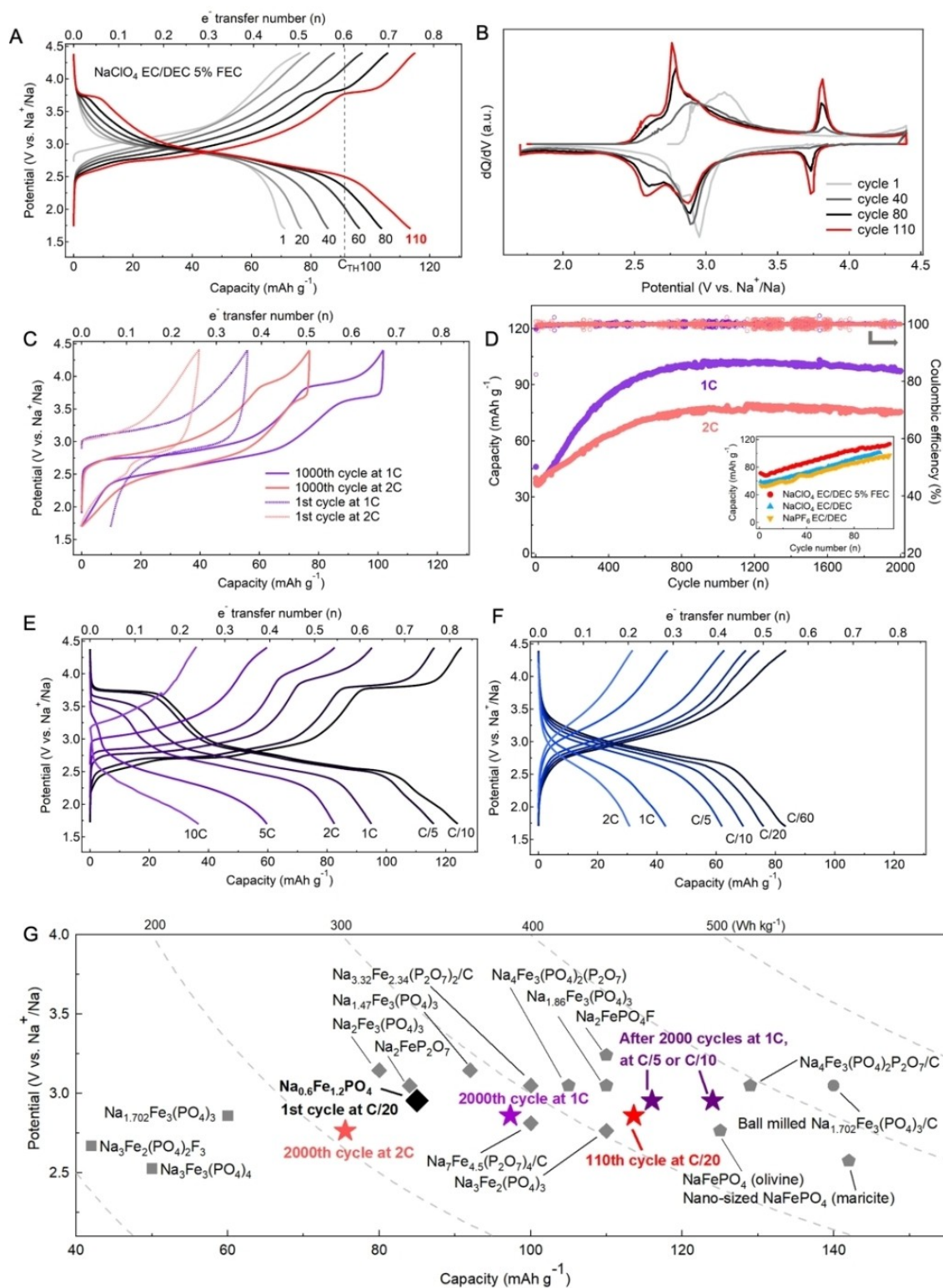
Figure 2. A) Potential vs. capacity profiles at a cycling rate of C/20 (C_{TH} = 91 mAh g^{-1}) and B) the corresponding dQ/dV plots, for the $Na_{0.6}Fe_{1.2}PO_4$ electrode using $NaClO_4$ in EC/DEC with 5 vol% FEC. C) Potential vs. capacity profiles of the first and the 1,000th cycle at a rate of 1 C and 2 C. D) The corresponding long-term cycling stability with inset showing data for other electrolyte formulation, cycling performed at a rate of C/20. Potential vs. capacity profiles at different C-rate for E) activated material after 2000 cycles at 1 C, and F) of pristine material. G) Energy density comparison (performances considered at the material level) of various iron phosphate-based cathode materials for SIBs.[10b,c,11a,13,19]

could be one explanation, however, this cannot support the fact that the theoretical capacity of 0.6Na is exceeded.

We thus turned our attention to the chemical environment during cycling and found that all cells containing reactive

fluoride species (e.g., PF_6^-, FEC) systematically displayed rapid and obvious capacity increase and the development of the 3.8 V redox process from the pristine $Na_{0.6}Fe_{1.2}PO_4$ (Figures 2A, S3C and S5A, C). In the absence of these, electrochemical activation of $Na_{0.6}Fe_{1.2}PO_4$ was also observed, assigned to fluoride generation from the anodic (or cathodic) decomposition of PTFE binder (Figures S3A, S6). In absence of any fluoride precursors (e.g., no PTFE, and using $NaClO_4$ in EC/DEC as electrolyte), no obvious activation could be observed over the course of the experiments, implying that fluoride has an important role here, whereas not excluding the involvement of other anionic species. Partial structural re-organization accompanied by fluoride insertion into the lattice, yielding a new composition, of $Na_{0.6+x}Fe_{1.2}PO_4F_x$ stoichiometry, can be thus accounted for the observed electrochemical evolution with cycling.

To further understand the electrochemical activation mechanism, in situ and ex situ XRD analyses were performed. In situ PXRD data was collected during the charge and discharge processes at C/30 for the first and second cycles (Figure 3A). During the sodium extraction process, the main diffraction peaks shift to higher 2θ angles, and the process is reversible upon sodiation. No significant diffraction pattern changes can be seen after two cycles corroborating the high stability and efficiency at these early stages of cycling. The desodiation/sodiation process is also found to proceed through a solid solution (single phase) system change. After the electrochemical activation process, a new diffraction pattern is revealed by ex situ XRD analysis (Figure 3B). Whereas certain diffraction peaks from the pristine phase are preserved ($2\theta=7°$) or appear shifted ($2\theta=7.95°$, $13.8°$, $15.2°$), a new series of peaks ($2\theta=7.5°$, $14.6°$) are evidenced. The quality of the ex-situ diffractograms did not allow us to perform any further crystalline analysis and the most plausible explanation is the in-operando

formation of a new, fluorinated phosphate phase with a high redox potential (e.g., $Na_{0.6+x}Fe_{1.2}PO_4F_x$). Further work is required to understand the formation and composition of this peculiar phase as other than operating at a high redox potential, it also exhibits much improved cycling stability and rate capability (Figure 2).

Conclusion

The $Na_{0.6}Fe_{1.2}PO_4$ prepared and analysed in this work not only shows improved electrochemical performances, but also a peculiar electrochemical activation process, yielding a new, high voltage phase with a redox potential of 3.8 V (vs. Na^+/Na). Whereas it is not possible at this stage to unambiguously clarify the structure, or the mechanism behind its formation, it remains interesting to understand this material, to then prepare this phase by chemical means. Despite these fundamental questions remained, the material we explore in this work achieves reversible capacities as high as 110 mAh g^{-1}, displays excellent rate capability, and stability on long long-term cycling, outperforming many of this type of cathode materials in literature (Figure 2G). The results in this work are encouraging to merit further investigation of this low-cost, safe and eco-friendly cathode material.

Experimental Section

Sample preparation

The $Na_{0.6}Fe_{1.2}PO_4$ was synthesized via a solid-state reaction with precursors processing by high-energy ball milling. The stoichiometric amounts of Na_2CO_3 ($\geq$ 99.5 %, Sigma-Aldrich), $NH_4H_2PO_4$ (99$^+$%, Acros Organics) and $FeC_2O_4 \cdot 2H_2O$ (99 %, Sigma-Aldrich), around 3.6 g in total, were first ball milled at 30 Hz for 20 min three times, with 20 min pause intervals under Ar atmosphere, using one stainless steel ball (25 mm diameter) in a 50 mL jar and high-energy miller (Ball Mill BM500, Anton Paar). To obtain very fine powder precursors, the jar was opened, and the caked precursors were scraped of the walls using a spatula, followed by and additional ball milling step at 15 Hz for 10 min under Ar atmosphere. The precursors were transferred into alumina crucibles and annealed at 550 °C for 12 h under Ar flow (99.99 % in purity) in a tubular furnace. The heating rate was 2 °C min^{-1} whereas the cooling was left to proceed naturally. The samples were transferred into a glovebox (MBraun, < 0.1 ppm O_2 and H_2O) with minimal exposure to air and stored therein for further analyses.

Characterization

Powder XRD (STOE DARMSTADT StadiP Transmission diffractometer system) equipped with a Mo cathode – $K_{\alpha 1}$ radiation ($\lambda =$ 0.71073 Å). ^{57}Fe Mössbauer spectra were recorded at room temperature in transmission geometry mode with a constant acceleration mode conventional Wissel Mössbauer spectrometer equipped with a ^{57}Co(Rh) radioactive source, a Reuter Stokes proportional counter detector and a CMCA-550 multichannel analyzer. All isomer shifts in Mössbauer spectra are given respective to α-Fe. Fourier transform infrared spectroscopy (FTIR) was carried out on pristine powders and spectra were recorded with a Shimadzu FTIR-8400S
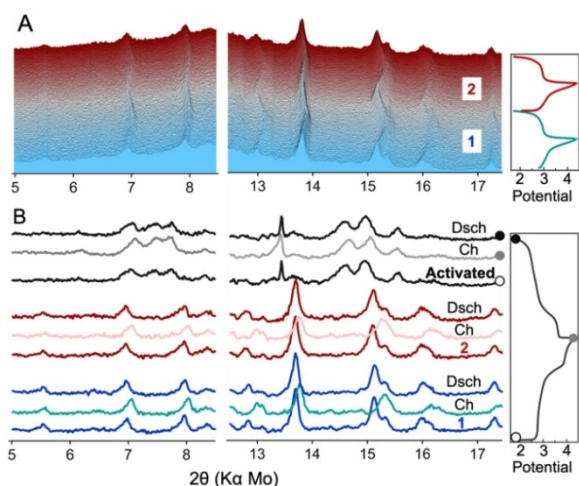

Figure 3. A) In situ XRD patterns and corresponding potential profiles for the $Na_{0.6}Fe_{1.2}PO_4$ electrode at the first and second cycles. B) XRD patterns for before the cycle, charge (Ch) and discharge (Dsch) states from the in situ XRD at the first (blue) and second (red) cycles and ex situ XRD for activated electrodes collected from disassembled coin cells after test at 1 C for 2000 cycles (black).

Batteries & Supercaps

Research Article
doi.org/10.1002/batt.202100390

Chemistry Europe
European Chemical
Societies Publishing

spectrophotometer. The microstructure and morphology were characterized by SEM (JEOL JSM 7600F) as well as TEM and EDX (Titan G2 60–300) after dispersing the samples on holey carbon film supported by a copper grid. The content of Na, Fe and P in the sample was measured by ICP (SPECTRO BLUE SOP, Spectro™).

In situ PXRD patterns were recorded using the same equipment as for PXPD data collection. The in situ coin cell assembly design is similar as to one presented in our previous work.[20] The working electrode was prepared by mixing $Na_{0.6}Fe_{1.2}PO_4$, Super P and PTFE with a composition ratio of $70:25:5$ wt% (7 mg in total). This composite was then pressed at 8 tons on an Al mesh current collector. Sodium metal disk was used as negative electrode, one sheet of glass fibre (Whatman, GF/D) as separator and 1 M $NaClO_4$ in EC/DEC containing 5 v% FEC as electrolyte.

Electrochemical cell assembly and analysis

The working electrodes were fabricated by dry grinding the samples (70 wt%) with super P carbon (SP) as conductive agent (25 wt%) and Poly tetra fluoroethylene (PTFE, powder, Sigma-Aldrich) as binder (5 wt%), followed by pressing the powder onto coin cell case. The typical mass loading was approximately 6–9 mg per square-cm. The electrochemical tests were performed in half cells (CR2032, SS316 coin cell format) with metallic Na as counter and reference electrode and one sheet of glass fiber (Whatman, GF/D) as separator. Different electrolyte formulations were used as received (DodoChem). The assembly was carried out in an Ar filled glove box (MBraun, <0.1 ppm O_2 and H_2O). Galvanostatic charge-discharge and CC-CV tests were performed on Neware battery testing system at ambient temperature.

Conflict of Interest

The authors declare no conflict of interest.

Data Availability Statement

The data that support the findings of this study are available from the corresponding author upon reasonable request.

[1] B. Dunn, H. Kamath, J.-M. Tarascon, *Science* **2011**, *334*, 928–935.

[2] N. Nitta, F. Wu, J. T. Lee, G. Yushin, *Mater. Today* **2015**, *18*, 252–264.

[3] a) D. Larcher, J. M. Tarascon, *Nat. Chem.* **2015**, *7*, 19–29; b) H. S. Hirsh, Y. Li, D. H. S. Tan, M. Zhang, E. Zhao, Y. S. Meng, *Adv. Energy Mater.* **2020**, *10*, 2001274.

[4] M. D. Slater, D. Kim, E. Lee, C. S. Johnson, *Adv. Funct. Mater.* **2013**, *23*, 947–958.

[5] a) Q. Zhu, J. Wang, X. Liu, N. Ebejer, D. Rambabu, A. Vlad, *Angew. Chem. Int. Ed. Engl.* **2020**, *59*, 16579–16586; b) X. Liu, S. Depaifve, T. Leyssens, S. Hermans, A. Vlad, *Batteries & Supercaps* **2019**, *2*, 1016–1025.

[6] Y. Li, Y. Lu, C. Zhao, Y.-S. Hu, M.-M. Titirici, H. Li, X. Huang, L. Chen, *Energy Storage Mater.* **2017**, *7*, 130–151.

[7] B. Song, G. M. Veith, J. Park, M. Yoon, P. S. Whitfield, M. J. Kirkham, J. Liu, A. Huq, *Chem. Mater.* **2018**, *31*, 124–134.

[8] a) K. Zaghib, J. Trottier, P. Hovington, F. Brochu, A. Guerfi, A. Mauger, C. M. Julien, *J. Power Sources* **2011**, *196*, 9612–9617; b) A. Sun, F. R. Beck, D. Haynes, J. A. Poston, S. R. Narayanan, P. N. Kumta, A. Manivannan, *Mater. Sci. Eng. B* **2012**, *177*, 1729–1733.

[9] a) C. Heubner, S. Heiden, M. Schneider, A. Michaelis, *Electrochim. Acta* **2017**, *233*, 78–84; b) Y. Zhu, Y. Xu, Y. Liu, C. Luo, C. Wang, *Nanoscale* **2013**, *5*, 780–787; c) Y. Liu, N. Zhang, F. Wang, X. Liu, L. Jiao, L.-Z. Fan, *Adv. Funct. Mater.* **2018**, *28*, https://onlinelibrary.wiley.com/doi/abs/10.1002/adfm.201801917.

[10] a) H. Kim, R. A. Shakoor, C. Park, S. Y. Lim, J.-S. Kim, Y. N. Jo, W. Cho, K. Miyasaka, R. Kahraman, Y. Jung, J. W. Choi, *Adv. Funct. Mater.* **2013**, *23*, 1147–1155; b) H. Kim, I. Park, S. Lee, H. Kim, K.-Y. Park, Y.-U. Park, H. Kim, J. Kim, H.-D. Lim, W.-S. Yoon, K. Kang, *Chem. Mater.* **2013**, *25*, 3614–3622; c) R. Rajagopalan, B. Chen, Z. Zhang, X. L. Wu, Y. Du, Y. Huang, B. Li, Y. Zong, J. Wang, G. H. Nam, M. Sindoro, S. X. Dou, H. K. Liu, H. Zhang, *Adv. Mater.* **2017**, *29*, https://onlinelibrary.wiley.com/doi/10.1002/adma.201605694.

[11] a) M. Chen, L. Chen, Z. Hu, Q. Liu, B. Zhang, Y. Hu, Q. Gu, J. L. Wang, L. Z. Wang, X. Guo, S. L. Chou, S. X. Dou, *Adv. Mater.* **2017**, *2*, https://onlinelibrary.wiley.com/doi/10.1002/adma.201605535; b) Y. Niu, M. Xu, C. Cheng, S. Bao, J. Hou, S. Liu, F. Yi, H. He, C. M. Li, *J. Mater. Chem. A* **2015**, *3*, 17224–17229; c) X. Zhu, T. Mochiku, H. Fujii, K. Tang, Y. Hu, Z. Huang, B. Luo, K. Ozawa, L. Wang, *Nano Res.* **2018**, *11*, 6197–6205.

[12] H. Li, M. Xu, Z. Zhang, Y. Lai, J. Ma, *Adv. Funct. Mater.* **2020**, *2000473*.

[13] J. Lu, S.-I. Nishimura, A. Yamada, *Electrochem. Commun.* **2017**, *79*, 51–54.

[14] a) N. V. Kosova, V. R. Podugolnikov, E. T. Devyatkina, A. B. Slobodyuk, *Mater. Res. Bull.* **2014**, *60*, 849–857; b) C. M. Burba, R. Frech, *Spectrochim. Acta Part A* **2006**, *65*, 44–50; c) C. Murugesan, S. Lochab, B. Senthilkumar, P. Barpanda, *ChemCatChem* **2018**, *10*, 1122–1127.

[15] A. Ait Salah, P. Jozwiak, K. Zaghib, J. Garbarczyk, F. Gendron, A. Mauger, C. M. Julien, *Spectrochim. Acta Part A* **2006**, *65*, 1007–1013.

[16] R. Rupp, A. Vlad, *J. Electrochem. Soc.* **2019**, *166*, A3122–A3131.

[17] S. Ko, Y. Yamada, A. Yamada, *Joule* **2021**, *5*, 998–1009.

[18] a) L. Zhang, D. Batuk, G. Chen, J.-M. Tarascon, *Electrochem. Commun.* **2017**, *77*, 81–84; b) L. Zhang, D. Dambournet, A. Iadecola, D. Batuk, O. J. Borkiewicz, K. M. Wiaderek, E. Salager, M. Shao, G. Chen, J.-M. Tarascon, *Chem. Mater.* **2018**, *30*, 5362–5372.

[19] a) D. Liu, G. T. R. Palmore, *ACS Sustainable Chem. Eng.* **2017**, *5*, 5766–5771; b) K. Chihara, A. Kitajou, I. D. Gocheva, S. Okada, J.-I. Yamaki, *J. Power Sources* **2013**, *227*, 80–85; c) G. S. Shinde, R. Gond, M. Avdeev, C. D. Ling, R. P. Rao, S. Adams, P. Barpanda, *Mater. Res. Express* **2019**, *7*, https://iopscience.iop.org/article/10.1088/2053-1591/ab54f4; d) K. Walczak, A. Kulka, J. Molenda, *Solid State Sci.* **2019**, *87*, 21–26; e) P. Barpanda, L. Lander, S.-i. Nishimura, A. Yamada, *Adv. Energy Mater.* **2018**, *8*; f) P. Barpanda, T. Ye, S.-I. Nishimura, S.-C. Chung, Y. Yamada, M. Okubo, H. Zhou, A. Yamada, *Electrochem. Commun.* **2012**, *24*, 116–119; g) W. Gao, Y. Niu, R. Zhan, Y. Wang, J. Jiang, J. Yang, M. Xu, *J. Alloys Compd.* **2019**, *771*, 297–301; h) Q. Li, Z. Liu, F. Zheng, R. Liu, J. Lee, G. L. Xu, G. Zhong, X. Hou, R. Fu, Z. Chen, K. Amine, J. Mi, S. Wu, C. P. Grey, Y. Yang, *Angew. Chem. Int. Ed. Engl.* **2018**, *57*, 11918–11923; i) X. Pu, H. Wang, T. Yuan, S. Cao, S. Liu, L. Xu, H. Yang, X. Ai, Z. Chen, Y. Cao, *Energy Storage Mater.* **2019**, *22*, 330–336; j) R. Essehli, H. Ben Yahia, K. Maher, M. T. Sougrati, A. Abouimrane, J. B. Park, Y. K. Sun, M. A. Al-Maadeed, I. Belharouak, *J. Power Sources* **2016**, *324*, 657–664; k) S.-M. Oh, S.-T. Myung, J. Hassoun, B. Scrosati, Y.-K. Sun, *Electrochem. Commun.* **2012**, *22*, 149–152; l) Y. Liu, N. Zhang, F. Wang, X. Liu, L. Jiao, L.-Z. Fan, *Adv. Funct. Mater.* **2018**, *28*, 1801917.

[20] L. Sieuw, A. E. Lakraychi, D. Rambabu, K. Robeyns, A. Jouhara, G. Borodi, C. Morari, P. Poizot, A. Vlad, *Chem. Mater.* **2020**, *32*, 9996–10006.